Inhibition of Localized Corrosion of Hot Dip Galvanised Steel by Phenylphosphonic Acid

C. F. Glover [a,z] and G. Williams[b]

[a]SPECIFIC, Baglan innovation Centre, Central Avenue, Baglan Energy Park, Baglan, Port Talbot SA12 7AX, United Kingdom

[b]Materials Research Centre, College of Engineering, Swansea University, Bay Campus, Skewen, Swansea SA1 8EN, United Kingdom

[z]E-mail: c.f.glover@swansea.ac.uk

Abstract

Phenylphosphonic acid (H_2PP) is investigated as a corrosion inhibitor of hot dip galvanised steel (HDG) fully immersed in a 5% (w/v) sodium chloride electrolyte. An *in-situ* Scanning Vibrating Electrode Technique (SVET) is used where concentrations of H_2PP are systematically added to the electrolyte in neutral conditions. H_2PP, at a concentration of $5x10^{-2}$ mol dm^{-3}, is shown to effectively inhibit localised corrosion over a 24 h period with 96% efficiency. H_2PP is compared with a sodium phosphate (Na_3PO_4) inhibitor at the same concentration over a wide pH range.

Manuscript submitted April 12, 2017; revised manuscript received May 24, 2017.
Published xx xx, xxxx.

1. Introduction

With current legislative pressure to eliminate Cr(vi)-based inhibitors from protective coating formulations, there is a pressing need to identify effective, environmentally-friendly alternatives. Chromate-free passivation treatments have been studied extensively [1–4] and the most widely used alternative to chromate is a phosphate passivating treatment. Such a system facilitates the precipitation of protective zinc compounds via the supply of soluble anions that react with the zinc ions generated in metal dissolution [5]. A phosphate passivation treatment generates a $Zn_3(PO_4)_2$ barrier to inhibit the anodic process[4-5], the formation of which can act to extend the pH stability of the surface layer down to values of around pH 6. However, as zinc phosphates are 1000 times more soluble than Cr (III), inferior corrosion inhibition performance is observed [7]. The corrosion of a zinc surface generates a wide range of pH zones, whether in bulk electrolyte conditions, atmospheric conditions or, most notably, under a water droplet [8,9]. Corrosion-driven cathodic coating delamination phenomena produces an alkaline underfilm environment where values of pH 10-11.5 have been recorded previously on a coated zinc surface [10]. In order to compete with an adsorbed chromium (III) oxide layer, an effective corrosion inhibitor system would have to be stable in a range of pH 4-14 [7]. It is therefore of great importance to examine potential chromate replacement inhibitors in non-neutral conditions.

In a recent Scanning Kelvin probe study, we showed that in-coating additions of H_2PP increased the initiation time for underfilm cathodic coating delamination by up to 20 h and reduced the delamination rate by up to 94% on hot dip galvanised steel (HDG) surfaces [11]. An ‘etch’ effect was shown to be the dominant inhibition mechanism, whereby a reaction occurs at the point of first contact of the wet coating with the substrate producing an interfacial metal phosphate salt layer. We hypothesise that a

second mode of inhibition occurs whereby the leaching of dissociated PP^{2-} ions from the coating into the substrate/coating interface forms a ZnPP layer, blocking the anodic reaction. H_2PP has been shown previously to strongly adsorb onto surface oxide films, disfavouring chloride [12]. The principal aim of this work is to determine the efficiency of H_2PP as an inhibitor for HDG surfaces in bulk immersion conditions. The localised corrosion activity occurring over a commercial grade HDG surface immersed in aqueous sodium chloride electrolyte has been mapped using *in situ* SVET, which has been widely used in previous corrosion studies [13–22]. The effect of concentration and pH on corrosion inhibition by H_2PP and an inorganic inhibitor, namely sodium phosphate (Na_3PO_4), are assessed. A pH of 11.5 has been chosen to mimic the underfilm conditions found in a corrosion-driven delamination cell. Neutral and acidic, pH 2, conditions have also been assessed.

2. Experimental

Materials: All HDG steel was supplied by Tata Steel UK and comprised of 0.7 mm gauge mild steel coated on both side with a 20 µm zinc layer cut into 50 mm x 50 mm square coupons. All chemicals were supplied by Sigma-Aldrich Chemical Co. and were of analytical grade purity.

Sample preparation: Prior to each experiment, abrasive cleaning was carried out using an aqueous slurry of 5 µm polishing alumina followed by washing with aqueous surfactant and finally rinsing with distilled water and then ethanol. For SVET and open circuit potential (OCP) experiments, samples were then prepared for immersion by being completely covered using 90 µm thick extruded PTFE 5490 tape (3M Ltd.), leaving exposed only the 9 mm x 9 mm experiment area on one face. All experimental electrolyte was prepared using analytical grade reagents obtained from

Aldrich Chemical Co. and distilled water. Solution pH was adjusted by the drop-wise addition of either HCl (aq) or NaOH (aq).

Methods: Measurements using the SVET were carried out using a probe comprising a Pt wire sealed in a glass sheath with a total tip diameter of ~ 225 μm and a 125 μm diameter Pt micro-disc electrode as the active region. A probe vibration frequency of 140 Hz and peak-to-peak vibration amplitude (A_{pp}), as measured stroboscopically in air, was 30 ± 5 μm. SVET instrument design, mode of operation and calibration can be found elsewhere [23]. Briefly, by Ohm's law, the peak-to-peak SVET voltage signal (V_{pp}) is related to the current flux density along the axis of probe vibration (j_z) by:

$$V_{pp} = j_z (A_{pp}/\kappa) \quad (1)$$

where κ is solution conductivity such that a quantity $G = \kappa/A_{pp}$ may be defined as the SVET calibration factor. The SVET calibration was checked galvanostatically in NaCl (aq) electrolyte of different concentrations using a specially devised two-compartment cell. Each compartment contained a 1 cm^2 Pt electrode and the two compartments were linked by a vertically orientated, electrolyte-filled glass tube of length 70 mm and of internal diameter 5 mm. During calibration, the SVET probe was inserted a distance of ca. 5 mm downward into the tube lumen. At this position, the current flux density was constant across the tube diameter and equal to the cell current divided by the internal area of cross section (minus the cross-sectional area of the SVET probe). Furthermore, the current flux was aligned vertically i.e. parallel with the tube axis and parallel with the axis of probe vibration. At all electrolyte concentrations and for $j_z = -15$ A/m^2 to 15 A/m^2 plots of V_{pp} vs. j_z gave good straight lines (correlation co-efficient > 0.998) and the values of G obtained from plot gradients agreed with those calculated using Equation (1) to within ± 10%.

In all cases samples were fully immersed, exposed area uppermost, in 5% NaCl (aq) electrolyte containing the relevant amount of phenyl phosphonic acid or sodium phosphate. The electrolyte bath was left unstirred and in contact with room air at a nominal temperature of 20°C. The SVET probe was held vertically and scanned at a fixed height of 100 μm above the metal surface. Scans were carried out immediately following immersion and at half-hourly intervals over a period of 24 h where a typical area of 9 mm x 9 mm was scanned. SVET experiments were carried out three times and representative data is presented. Time-dependent free corrosion potential measurements were performed using a Solartron SI 1280B Electrochemical Workstation.

Mass loss experiments were carried out by first cutting the HDG material into a coupon of approximately 20 mm x 20 mm. Coupons were then cleaned and weighed and subsequently taped using 90 μm thick extruded PTFE 5490 tape (3M Ltd.) leaving a 10 mm x 10 mm exposed surface. Samples were then fully immersed in the relevant electrolyte for a period of one week. Samples, still taped, were then immersed in an etchant (made up of 50 ml H_3PO_4, 20 g CrO_3 and 1 L H_2O)[24] at a temperature of ca. 80^{o}C for a period of 5 min. All taping was then removed and samples were cleaned using ethanol and oven-dried at ca.100^{o}C for 10 min. All samples were then weighed again. In each case experiments were carried out in triplicate.

For calculating the solubility product (Ksp) of the ZnPP salt, titrations were carried out where $ZnCl_{2(aq)}$ solutions, of various concentrations, were titrated from a burette

into a beaker containing 10 ml of aqueous solution containing various concentrations of H_2PP adjusted to pH 7. The volume of $ZnCl_{2(aq)}$ solution required to produce soluble product in the beaker was recorded and the concentrations of Zn^{2+} (aq) and PP^{2-} (aq) used to give an estimate of Ksp.

3. Results and discussion

Corrosion inhibition of hot dip galvanised steel by phenyl phosphonic acid in neutral conditions

A baseline for the current density distributions, as a function of time, above the surface of unpolarised HDG samples freely corroding in uninhibited 5% wt/v NaCl (aq) at pH 7 was established using an *in situ* SVET. Representative current density maps obtained at times between 1 h and 24 h, after initial sample immersion, are shown in Figure. 1. It can be observed that corrosion activity occurs with the development of a single anode and a single cathode. For the duration of the 24 h experiment, the large cathode occupies roughly one third of the experiment area and the anode remains localised throughout. The photographic image presented in Figure. 1(f) shows white rust corresponding to the anodic region observed on the current density maps. The principal anodic and cathodic processes that occur on a freely corroding Zn surface in solutions of neutral pH are:

$$Zn \rightleftharpoons Zn^{2+} + 2e^- \quad (2)$$

$$O_2 + 2H_2O + 4e^- \rightleftharpoons 4OH^- \quad (3)$$

Respective current density maps for SVET experiments carried out in electrolyte with H_2PP concentrations $1x10^{-3}$ mol dm^{-3}, $1x10^{-2}$ mol dm^{-3}, and $5x10^{-2}$ mol dm^{-3} in neutral conditions are given in Figures. 2 and 3. Although anodic activity is significantly

reduced in comparison with the control experiment, for the lower H_2PP concentrations of $1x10^{-3}$ mol dm^{-3}, $1x10^{-2}$ mol dm^{-3}, inhibition is incomplete. This is illustrated in both cases by the presence of a large local anode. However, the anode size and intensity appears to reduce with increasing H_2PP concentration. Photographic images, given in part Figure 2(d) and Figure 3(a)ii, show that the Zn surface has been stripped away in a small region corresponding to the local anodic activity on the current density maps. In both cases a protective film can be observed on the non-corroded area of the sample. At a concentration of $5x10^{-2}$ mol dm^{-3} H_2PP, complete inhibition was achieved where no corrosion activity can be observed on the current density maps (Figure. 3(b)i) and no surface tarnishing is visible in the corresponding photograph (Figure 3(b)ii).

(Figure 1)

(Figure 2)

(Figure 3)

Area-averaged, integrated SVET-derived anodic current density (J_{at}) data, plotted as a function of time for all H_2PP concentrations tested, is given in Figure 4(a). The data was obtained by the numerical area integration of j_z distributions to give an estimation of time-dependent total local corrosion currents. A progressive decrease in J_{at} with increasing concentrations of H_2PP can be observed. Using J_{at} values, the total equivalent Zn loss is calculated using:

$$\frac{\mathbf{J_{at}.t}}{\mathbf{F}} . \frac{\mathbf{A_r(Zn)}}{\mathbf{2}}$$

where F is Faradays constant. Zn loss (gm^{-2}) measurements after 24 h immersion are presented in Figure 4(b) showing a progressive reduction of Zn dissolved from the sample with increasing H_2PP concentration.

Inhibition efficiency (%) of H_2PP can be calculated using the following equation:

$$\textbf{Inhibition efficieny}\ (\%) = \frac{\textbf{mass loss}_c - \textbf{mass loss}_i}{\textbf{mass loss}_c}\ \textbf{x 100} \qquad (5)$$

where 'mass $loss_c$' and 'mass $loss_i$' are the total mass of Zn lost after the 24 h immersion time in control conditions and inhibited conditions respectively. An efficiency of ca. 96% is calculated for H_2PP additions at a concentration of $5x10^{-2}$ mol dm^{-3}.

(Figure 4)

Figure 5 shows data plots for open circuit potential (OCP) measurements of bare HDG in 5% wt/v NaCl (aq) solution at neutral pH where H_2PP was present in concentrations ranging from $1x10^{-3}$ to $5x10^{-2}$ mol dm^{-3}. The eventual value of the control result, represented by the dashed line, displays an E_{corr} value near the equilibrium value of Zn. In the presence of H_2PP, at the lowest concentrations of $1x10^{-3}$ mol dm^{-3}, no significant effect on the final potential is observed.

(Figure 5)

For H_2PP concentrations of $\geq 1x10^{-3}$mol dm^{-3}, the initial period up to ca. 100 min indicates predominant net cathodic inhibition. This suggests that low level anodic activity, distributed over large areas of the exposed surface, is galvanically coupled with intense cathodic sites. Beyond 100 min the highest H_2PP concentration (shown in plot (i)) rapidly increases to more positive E_{corr} values. A high pH zone in the vicinity of a local cathode would convert bulk $HPP^{-}_{(aq)}$ anions to $PP^{2-}_{(aq)}$. Zn^{2+} ions

produced by reaction (1) can migrate to the sites of local cathodic activity, combining with free PP^{2-} anions, to form an insoluble Zn(PP) film thus stifling ongoing interfacial electron transfer. Figure 6(a-c) gives a schematic representation of these processes.

(Figure 6)

pH Dependence of a phenyl phosphonic acid inhibitor

The inhibition efficiency of H_2PP added to bulk electrolyte at a concentration of $5x10^{-2}$ mol dm^{-3} and adjusted to pH 2 and pH 11.5 is investigated. To obtain baseline information, the corrosion occurring on bare HDG in uninhibited conditions is first characterised. Results from experiments carried out at pH 2 are given in Figure 7. In contrast to the localised corrosion activity observed in neutral conditions, general corrosion activity can be observed. Due to a lack of OH^- in the acidic electrolyte, no 'white rust' corrosion product is observed in the photographic image given in Figure 7(d) showing the sample surface after 24 h immersion. Instead, a tarnishing of the surface corresponding to the anodic regions visible in the current density surface maps is evident. In acidic solutions, the active form of corrosion occurring is controlled by the cathodic reaction. This is predominantly hydrogen evolution[9], as per the following reaction:

$$2H^+ + 2e^- \rightleftharpoons H_2 \qquad (6)$$

(Figure 7)

Likewise, SVET surface plots for the inhibited case shown in Figure 8 indicate general corrosion by the highly interspersed anodic and cathodic regions. Anodic regions appear to be more intense than the uninhibited case.

(Figure 8)

Summary plots of area-averaged, integrated SVET-derived J_{at} vs. time profiles for samples immersed in electrolyte containing no inhibitor, $1x10^{-2}$ $moldm^{-3}$ H_2PP and $5x10^{-2}$ mol dm^{-3} H_2PP at pH 2 and pH 11.5 are given in Figure 9(a) and (b) respectively. For experiments carried out in pH 2, at the highest H_2PP concentration, J_{at} is initially less than that of the uninhibited experiment but, after approximately 17 h, J_{at} progressively increases to extremely high values. At the lower H_2PP concentration very little corrosive activity was observed. Due to the generalised nature of the corrosion at this pH, the accuracy of these findings is in question and will be discussed in more detail later.

(Figure 9)

In uninhibited conditions adjusted to pH 11.5, a single cathode and single anode situation prevails as with neutral conditions. However, as illustrated in Figure 10, after a 5 h period of a fixed local peak, anodic activity can be seen to spread in a wave-like manner across the substrate so the anodic and cathodic regions each occupy approximately half the experiment area. The appearance of the sample surface is depicted in the photographic image given in Figure 10(d) where the paler areas correspond with the anodic region shown in Figure 10(a-c). At pH 11.5, there is an increased thermodynamic likelihood that precipitation of an insoluble corrosion product will occur, such as zinc hydroxoxychlorides, resulting in a relocation of the anodic and cathodic sites [9].

(Figure 10)

Inhibited experiments carried out in pH 11.5 show that a strong anodic peak forms on the sample surface then passivates after ca. 6 h (Figure 11). Further anodic activity is shown to occur at ca. 22 h as shown in Figure 11(c). The photographic image given in Figure 11(d) reveals the substantial amount of corrosion product formed on the sample surface. The J_{at} summary plot given in Figure 9(b) shows that, as the H_2PP concentration is increased, the J_{at} is progressively decreased. However, at the higher concentration of H_2PP, it can be observed that intense localised anodic activity occurs in between periods of total inhibition. This is shown by the anodic spikes that initiate at immersion times of approximately 2 h and 22 h and remain for approximately 3 h. We suggest that, in alkaline conditions, H_2PP acts as an adsorption inhibitor whereby the PP^{2-} anion adsorbs onto the HDG surface and reinforces the $Zn(OH)_2$ layer. This layer disfavours Cl^- adsorption preventing attack. The periods of intense, highly localised, anodic activity indicate that this layer is only partially protective.

By considering the H_2PP species present in electrolyte in different pH conditions, we can further understand the mechanism by which the inhibitor is acting. Phosphorus oxyacids undergo a series of stepwise deprotonations and, with each step; a progressively higher pK_a is exhibited. The pK_a values for H_2PP are 2.3 and 7.8 [25]. The deprotonation equilibria for H_2PP are as follows [25]:

$$H_2PP_{(aq)} \rightleftharpoons HPP^-_{(aq)} + H^+_{(aq)} \qquad (pK_{a1} = 2.3) \qquad (7)$$

$$HPP^-_{(aq)} \rightleftharpoons PP^{2-}_{(aq)} + H^+_{(aq)} \qquad (pK_{a2} = 7.8) \qquad (8)$$

The following equation can be used to calculate the $[Zn^{2+}]$ threshold at which ZnPP will precipitate:

$$[Zn^{2+}(aq)][PP^{2-}(aq)] = ksp \qquad (9)$$

where ksp is the solubility product calculated to be $1x10^{-6}$ mol^2dm^{-6} through a series of titrations.

Under aqueous conditions, the pH-dependent concentration of PP^{2-} ($[PP^{2-}]$) is given by:

$$[\mathbf{PP^{2-}}] = \frac{[\mathbf{PP}]_{\mathbf{tot}}}{\mathbf{1} + \mathbf{10}^{(-\mathbf{pH}+\mathbf{7.8})} + \mathbf{10}^{(-\mathbf{2pH}+\mathbf{7.8}+\mathbf{2.3})}} \quad (10)$$

where $[PP]_{tot}$ is the total concentration of the phenyl phosphonate species. From Equation (10) it can be shown that $[PP^{2-}] = 6.8 \times 10^{-3}$ mol dm^{-3} $[PP]_{tot}$ at pH 7. By applying this value and the ksp value to Equation (9) a $[Zn^{2+}]$ threshold can be calculated for the precipitation of solid Zn(PP) where a value of 1.46×10^{-4} mol dm^{-3} is obtained.

According to the Pourbaix diagram for Zn [26], when Zn is immersed in solution of low pH, an abundance of Zn^{2+} ions would be present. By incorporating H_2PP in the same conditions, the HPP^- species would be prevalent, according to the pk_a value given in reaction (7). As such, it is expected that PP^{2-} levels would be insufficient to form a solid film despite the level of Zn^{2+} ions. This accounts for the drop in efficiency with increasingly acidic pH. At high pH levels, an increased supply of PP^{2-} would be expected in the electrolyte, according to Equation (8). However, the corrosion product formed at high pH, according to the Pourbaix diagram, is the highly soluble zincate anion (ZnO_2^{2-}). Therefore, even with sufficient PP^{2-}, without the presence of Zn^{2+} ions it would not be possible for a solid Zn(PP) film to form. As such, a decreased inhibition efficiency of H_2PP would be expected at increasingly alkaline pH, the results indicate this.

Corrosion inhibition of hot dip galvanised steel by sodium phosphate

283 Having identified an optimum H_2PP concentration value of $5x10^{-2}$ mol dm^{-3} for the
284 effective inhibition of a HDG surface, a comparative investigation assessed the
285 efficiency of a sodium phosphate (Na_3PO_4) inhibitor at this concentration. The
286 photographic image given in Figure 12(b)(ii), taken at 24 h immersion time, shows
287 that only partial inhibition is achieved in neutral conditions. A protective layer is
288 visible over the whole surface but localised corrosive metal attack can be observed in
289 a small, isolated area. This is confirmed by the anodic region shown in the
290 corresponding corner of the SVET-derived surface map of Figure 12(b)(i). Figure
291 13[a-c] summarises J_{at} vs. time data and it can be observed that values measured at pH
292 7 (Figure 13(b)) in the presence of Na_3PO_4 are much lower than those measured in
293 uninhibited conditions throughout the 24 h period.

294 As with H_2PP, incomplete inhibition was observed for experiments carried out in
295 alkaline conditions. Figure 12(c)(ii) shows the hydrolysed corrosion product formed
296 on the sample surface after 24 h when immersed in solution at pH 11.5. As with
297 experiments carried out at pH 7, all visible corrosion product is constrained to an
298 isolated region and the remainder of the surface is corrosion-free. However, the
299 SVET surface map shows several local anodes in a region covering half the
300 experiment area. Extremely low initial J_{at} values were recorded in the presence of
301 Na_3PO_4 (as shown in Figure 13(c)(ii)), this progressively increased to values matching
302 those measured in uninhibited conditions at ca. 15 h and continued to increase to
303 values of ca. 3.4 Am^{-2} over the 24 h period. This was in contrast to the uninhibited
304 experiment where J_{at} values were consistently in the region 1.25 Am^{-2} for the duration
305 of the 24 h experiment. Unlike the same experiment carried out with H_2PP, in the
306 presence of Na_3PO_4 no re-passivation of the surface is observed after the occurrence
307 of anodic activity where J_{at} values return to approximately 0 Am^{-2}.

No sign of inhibition is observed where experiments were carried out at pH 2 as the J_{at} values, given in 13(a), are substantially higher than that of the uninhibited case throughout the 24 h time period.

(Figure 12)

(Figure 13)

SVET-derived mass-loss data (Figure 14(a)) calculated using Equation (4) indicates that, in all cases, Zn mass loss is at a minimum when experiments were carried out in neutral conditions. In all pH conditions, additions of H_2PP appear to reduce Zn loss when compared with the uninhibited experiment. H_2PP additions were least effective in acidic conditions.

(Figure 14)

The results suggest that, at pH 7, Na_3PO_4 additions appear to significantly reduce Zn loss. However, in non-neutral conditions, additions of Na_3PO_4 increased Zn loss when compared to the uninhibited experiment. The results presented here indicate that Na_3PO_4 additions are less effective than H_2PP. To investigate this further, $[Zn^{2+}]$ threshold for the precipitation of solid $Zn_3(PO_4)_2$ is calculated. As described above, phosphorus oxyacids undergo a series of stepwise deprotonations and a progressively higher pK_a is exhibited with each step. The first, second and third pK_a values are 2.0, 6.9 and 12.3 respectively for Na_3PO_4[25]. The following equation can be used to calculate the $[Zn^{2+}]$ threshold at which $Zn_3(PO_4)_2$ will precipitate:

$$[Zn^{2+}]^3[PO_4^{3-}]^2 = ksp \quad (10)$$

where ksp is $9x10^{-33}$ mol^2dm^{-6} [27]. Under aqueous conditions, the pH-dependent concentration of PO_4^{3-} ($[PO_4^{3-}]$) is given by:

$$[PO_4^{3-}] = \frac{[PO_4]_{tot}}{1 + 10^{(-pH+12.5)} + 10^{(-2pH+12.5+6.9)} + 10^{(-3pH+12.5+6.9+2)}} \quad (11)$$

where $[PO_4]_{tot}$ is the total concentration of the phosphate species, which is $5x10^{-2}$ mol dm^{-3} in this case. Equation (11) may be used to show that $[PO_4^{3-}] = 8.8 \times 10^{-8}$. By applying this value and the ksp value to Equation (10) a $[Zn^{2+}]$ threshold can be calculated for the precipitation of solid $Zn_3(PO_4)_2$ where a value of 5.38×10^{-5} mol dm^{-3} is obtained. This is lower than the predicted $[Zn^{2+}]$ threshold value for the precipitation of ZnPP, which is 1.46×10^{-4} mol dm^{-3}; this result suggests that Na_3PO_4 should be the more effective inhibitor. However, it is proposed that the incomplete inhibition observed in this case, where availability of PO_4^{3-} is not limited, results from precipitation of $Zn_3(PO_4)_2$ in solution above the sites of anodic Zn dissolution and not directly on the corroding surface. This is represented schematically in Figure 15. Zn^{2+}, therefore, does not migrate to sites of local cathodic activity, as is the case with ZnPP (illustrated in Figure 6(b)), to instigate the deposition of blocking films of $Zn_3(PO_4)_2$ directly on these regions. This was observed previously by Williams et al where the effect of a phosphate inhibitor on a corroding magnesium surface was assessed [22].

(Figure 15)

Gravimetric mass-loss experiments

Results for gravimetric mass-loss experiments are given in Figure 14(b) generally show good correlation with most SVET-derived data. One exception is the uninhibited experiments carried out at pH 2 where a significantly higher value of Zn loss was recorded when compared to the SVET-derived data given in Figure 14(a). In

this instance, it appears that the anode-cathode separation distance is less than the 100 μm SVET probe height such that the current flux lines do not cross the plane of scan and are not detected by the SVET [28]. If Zn-loss data in uninhibited conditions at pH 2 has been underestimated by the SVET-derived data, it may be more realistic to suggest that Na_3PO_4 is simply ineffective at low pH rather than an accelerant of corrosion, as the results from the previous section suggest. Although SVET-derived J_{at} values obtained in uninhibited pH 2 conditions are not truly representative, the observation that a change from localised to general corrosion occurs is still an important result.

Gravimetric mass loss experiments carried out with $5x10^{-2}$ mol dm^{-3} H_2PP additions at pH 11.5 also showed significantly higher values (Figure 14(b)) when compared with the SVET-derived data (Figure 14(a)) obtained after 24 h immersion. The J_{at} vs. time profile given in Figure 9(b)iii indicates that the surface re-passivates for 17 h following intense and highly localised anodic activity, as shown in the current density surface maps given in Figure 11(a-c). Samples in the gravimetric mass loss experiment must be immersed in the corrosive environment for one week in order to make discernible weight-change measurements. As such, it is likely that, over this longer time period, the protective barrier is broken down to the point that no further passivation occurs leading to further corrosion activity. The photographic image of the sample surface (Figure 11(d)) after the SVET experiment shows hydrolysed corrosion product covering areas of the sample surface that do not correspond with any anodic features in the current density maps given in Figure 11(a-c). We suggest that either general corrosion is occurring in these areas and anodic activity has gone undetected by the SVET, or corrosion product has been produced from one small and

377 highly intense anodic region and subsequently moved through the electrolyte. In the
378 case of the latter, there would be no reason to suggest that the SVET-derived data is
379 not a true representative of the corrosion activity occurring on the sample surface over
380 24 h.

381

382 Inhibition efficiency (%) values, calculated using Equation 5 are listed in Table 1 for
383 both SVET-derived and gravimetric mass-loss values measured in p H 2, pH 7 and pH
384 11.5. The SVET-derived results show an efficiency of 96.3% for experiments carried
385 out in neutral conditions and, as would be expected, the general trend is for efficiency
386 to be reduced where pH is above and below neutral.

387

388 **Table. 1.** Values of inhibition efficiency when bare HDG samples are added to a 5%
389 (w/v) $NaCl_{(aq)}$ electrolyte adjusted to pH 2, pH 7 and pH 11.5 containing additions of
390 $5x10^{-2}$ mol dm^{-3} H_2PP or $5x10^{-2}$ mol dm^{-3} Na_3PO_4.

pH	Efficiency / %			
	H_2PP		Na_3PO_4	
	SVET-derived	Gravimetric	SVET-derived	Gravimetric
2	46.1	64.8	-54.6	35.0
7	96.3	75.1	75.0	60.4
11.5	89.5	34.0	-3.3	3.9

391

392 **4. Conclusions**

393 (a) Phenyl phosphonic acid (H_2PP) at a concentration of $5x10^{-2}$ mol dm^{-3} has been
394 shown to be 96% effective for the inhibition of corrosion on hot dip galvanised steel
395 (HDG) immersed in 5%wt/v NaCl (aq) electrolyte in neutral conditions.

396 (b) A combination of data from *in situ* scanning vibrating electrode technique (SVET)
397 and open circuit potential measurements indicate that a Zn(PP) salt film forms on
398 anodic sites facilitated by the conversion of bulk $HPP^{-}_{(aq)}$ anions to $PP^{2-}_{(aq)}$ occurring
399 at zones of high pH at cathodic sites.

(c) H_2PP efficiency is shown to be higher than that for sodium phosphate (Na_3PO_4) where an SVET-derived efficiency of 75% was calculated for additions at the same concentration. The substantially lower inhibition efficiency of Na_3PO_4 suggests that precipitation of $Zn_3(PO_4)_2$ does not occur directly on the corroding surface but rests in solution in the regions above.

(d) H_2PP is shown to be less effective as a corrosion inhibitor in non-neutral conditions. At low pH, an abundance of Zn^{2+} ions are present but the concentration of PP^{2-} is insufficient to form a solid film. At high pH a soluble zincate anion (ZnO_2^{2-}) tends to prevail. Despite an abundance of available PP^{2-} anions, Zn^{2+} levels are insufficient to combine with PP^{2-} anions to establish a homogenous protective layer.

5. Acknowledgements

The authors recognise the financial support of TATA Steel UK and the United Kingdom Engineering and Physical Sciences Research Council (EPSRC), Welsh Government and Innovate UK for the SPECIFIC Innovation and Knowledge Centre (grant numbers EP/I019278/1, EP/K000292/1, EP/L010372/1).

6. List of figures

Figure. 1. SVET-derived current density surface maps of unpolarised HDG obtained following immersion in aerated 5% (w/v) NaCl (aq) at pH 7 at time a) 1h b) 2 h, and c) 6 h where d) shows a photographic image of the sample after 24h immersion.

Figure. 2. SVET-derived current density surface maps of unpolarised HDG obtained following immersion in aerated 5% (w/v) NaCl (aq) at pH 7 containing $1x10^{-3}$ mol dm^{-3} H_2PP at times a) 30 min b) 6 h c) 24 h where d) is a photographic image of the sample after 24 h of immersion.

Figure. 3. i) SVET-derived current density surface maps of unpolarised HDG obtained following immersion in aerated 5% (w/v) NaCl (aq) at pH 7containing a) $1x10^{-2}$ mol dm^{-3} and b) $5x10^{-2}$ mol dm^{-3} H_2PP at time 20 h where ii) is a photographic image of the sample after 24 h of immersion.

Figure. 4. a) Area-averaged, integrated SVET-derived anodic current density vs. time profiles obtained for HDG immersed in aerated 5% (w/v) NaCl (aq) at pH 7

containing (i) $5x10^{-2}$ mol dm^{-3} (ii) $1x10^{-2}$ mol dm^{-3} (iii) $1x10^{-3}$ mol dm^{-3} H_2PP. Curve (iv) was obtained in the absence of inhibitor. b) Summary of measured corrosion mass loss over 24 h as a function of $[PP^{2-}]$.

Figure. 5. Plot of E_{corr} with respect to time for HDG immersed in aerated 5% wt/v NaCl (aq) electrolyte at pH 7 containing (i) $5x10^{-2}$ mol dm^{-3} (ii) $1x10^{-3}$ mol dm^{-3} (iii) $1x10^{-2}$ mol dm^{-3} H_2PP. The dashed line represents the eventual value obtained in the absence of inhibitor.

Figure. 6. Schematic representation of the mechanism of zinc corrosion inhibition by aqueous phenyl phosphonate ions at neutral pH, showing (a) localisation of the early stages of corrosion, (b) phosphonate speciation in the vicinity of the local cathode and (c) the deposition of an insoluble film.

Figure. 7. SVET-derived current density surface map of unpolarised HDG obtained following immersion in aerated 5% (w/v) NaCl (aq) adjusted to pH 2 at time a) 1h b) 14 h, and c) 24 h where d) shows a photographic image of the sample after 24h immersion.

Figure. 8. SVET derived current density surface map of unpolarised HDG obtained following immersion in aerated 5% (w/v) NaCl (aq) at pH 2 containing $5x10^{-2}$ mol $dm^{-3}H_2PP$ at (a) 30 mins, (b) 2.5 h, c) 22 h where (d) shows a photographic image of the sample after 24h immersion.

Figure. 9. Area-averaged, integrated SVET-derived anodic current density vs. time profiles obtained for HDG immersed in aerated 5% (w/v) $NaCl_{(aq)}$ with i) no H_2PP additions and H_2PP additions of ii) 10^{-2} mol dm^{-3} and iii) $5x10^{-2}$ mol dm^{-3} where the bulk pH of the experimental electrolyte has been altered to (a) pH 2 and (b) pH 11.5.

Figure.10. SVET derived current density surface map of unpolarised HDG obtained following immersion in aerated 5% (w/v) NaCl (aq) at pH 11.5 at time a) 1 h b) 6 h, c) 14 h where d) shows a photographic image of the sample after 24 h immersion.

Figure. 11. SVET derived current density surface map of unpolarised HDG obtained following immersion in aerated 5% (w/v) NaCl (aq) at pH 11.5 containing $5x10^{-2}$ mol dm^{-3} H_2PP at (a) 2 h, (b) 3.5 h, c) (e) 22 h where (d) shows a photographic image of the sample after 24h immersion.

Figure. 12. i) SVET-derived current density surface maps of unpolarised HDG obtained following immersion in aerated 5% (w/v) NaCl (aq) containing $5x10^{-2}$ mol dm^{-3} Na_3PO_4 after 24 h and ii) a photographic image of the sample after 24 h immersion where the bulk electrolyte was adjusted to a) pH 2, b) pH 7 and c) pH 11.5.

Figure. 13. Summary of area-averaged, integrated SVET-derived anodic current density versus time profiles obtained for HDG immersed in aerated 5% (w/v) NaCl (aq) containing i) no inhibitor and ii) $5x10^{-2}$ mol dm^{-3} PO_4^{3-} adjusted to a) pH 2 b) pH 7 and c) pH 11.5.

Figure. 14. Bar charts showing Zinc loss (gm^{-2}) from HDG samples after immersion in aerated 5% (w/v) $NaCl_{(aq)}$ at pH 2, pH 7 and pH 11.5 for additions of H_2PP and

472 Na_3PO_4 at a concentration of $5x10^{-2}$ mol dm^{-3}, and no inhibitor additions, obtained a)
473 using SVET after 24 h immersion and b) from actually mass loss experiments after
474 one week immersion.

475 Figure. 15. Schematic representation of a locally corroding HDG surface in the
476 presence of phosphate ions.

477 **6. References**

478 1. W. J. Vanooij and S. A, *Surf. Coatings Technol.*, **39**, 667–674 (1989).

479 2. K. Aramaki, *Corros. Sci.*, **43**, 2201–2215 (2001).

480 3. C. G. Da Silva, A. N. Correia, P. de Lima-Neto, I. C. P. Margarit-Mattos, and O.
481 R. Mattos, *Corros. Sci.*, **47**, 709–722 (2005).

482 4. S. Dalbin, G. Maurin, R. P. Nogueira, J. Persello, and N. Pommier, *Surf. Coatings*
483 *Technol.*, **194**, 363–371 (2005).

484 5. K. Aramaki, **43**, 591–604 (2001).

485 6. S. M. Powell, H. N. Mcmurray, and D. A. Worsley, **55**, 1040–1051 (1999).

486 7. S. Thomas, N. Birbilis, M. S. Venkatraman, and I. S. Cole, *Corros. Sci.*, **69**, 11–22
487 (2013)

488 8. N. S. Azmat, K. D. Ralston, B. C. Muddle, and I. S. Cole, *Corros. Sci.*, **53**, 1604–
489 1615 (2011)

490 9. S. Thomas, N. Birbilis, M. S. Venkatraman, and I. S. Cole, *Corrosion*, **68**, 1–9
491 (2012).

492 10. W. Fürbeth and M. Stratmann, *Prog. Org. Coatings*, **39**, 23–29 (2000).

493 11. C. F. Glover, R. Subramanian, and G. Williams, *J. Electrochem. Soc.*, **162**, C433–
494 C441 (2015).

495 12. A. J. Coleman, H. N. Mcmurray, G. Williams, A. Afseth, and G. M. Scamans, *J.*
496 *Electrochem. Soc.*, **10**, C35 - C38 (2007).

497 13. A. Alvarez-Pampliega et al., *Electrochim. Acta*, **61**, 107–117 (2012)

498 14. A. Alvarez-Pampliega et al., *Electrochim. Acta*, **102**, 319–327 (2013)

499 15. J. C. B. Bertoncello, S. M. Manhabosco, and L. F. P. Dick, *Corros. Sci.*, **94**, 359–
500 367 (2015).

501 16. J. R. Kish, G. Williams, J. R. McDermid, J. M. Thuss, and C. F. Glover, *J.*
502 *Electrochem. Soc.*, **161**, C405–C411 (2014).

503 17. J. J. Santana, J. González-Guzmán, J. Izquierdo, S. González, and R. M. Souto,
504 *Corros. Sci.*, **52**, 3924–3931 (2010).

505 18. M. Taryba et al., *Electrochim. Acta*, **56**, 4475–4488 (2011).

506 19. G. Williams, K. Gusieva, and N. Birbilis, *Corrosion*, **68**, 489–498 (2012).

507 20. B. P. Wilson, J. R. Searle, K. Yliniemi, D. a. Worsley, and H. N. McMurray,
508 *Electrochim. Acta*, **66**, 52–60 (2012).

509 21. A. C. Bastos, M. G. S. Ferreira, and A. M. Simões, *Prog. Org. Coatings*, **52**, 339–

350 (2005).

22. G. Williams, H. N. McMurray, and R. Grace, *Electrochim. Acta*, **55**, 7824–7833 (2010).

23. G. Williams and H. Neil McMurray, *J. Electrochem. Soc.*, **155**, C340 (2008).

24. T. H. Muster, W. D. Ganther, and I. S. Cole, *Corros. Sci.*, **49**, 2037–2058 (2007).

25. G. Williams, A. Gabriel, A. Cook, and H. N. McMurray, *J. Electrochem. Soc.*, **153**, B425 (2006).

26. M. Pourbaix, *Atlas of Electrochemical Equilibria in Aqueous Solutions, second ed., National Association of Corrosion Engineers, Houston*, (1974).

27. W. Stumm and J. J. Morgan, *Aquatic Chemistry: An Introduction Emphasizing Chemical Equilibria in Natural Waters*, Wiley, New York, 780, (1981).

28. G. Williams, A. J. Coleman, and H. N. McMurray, *Electrochim. Acta*, **55**, 5947–5958 (2010).

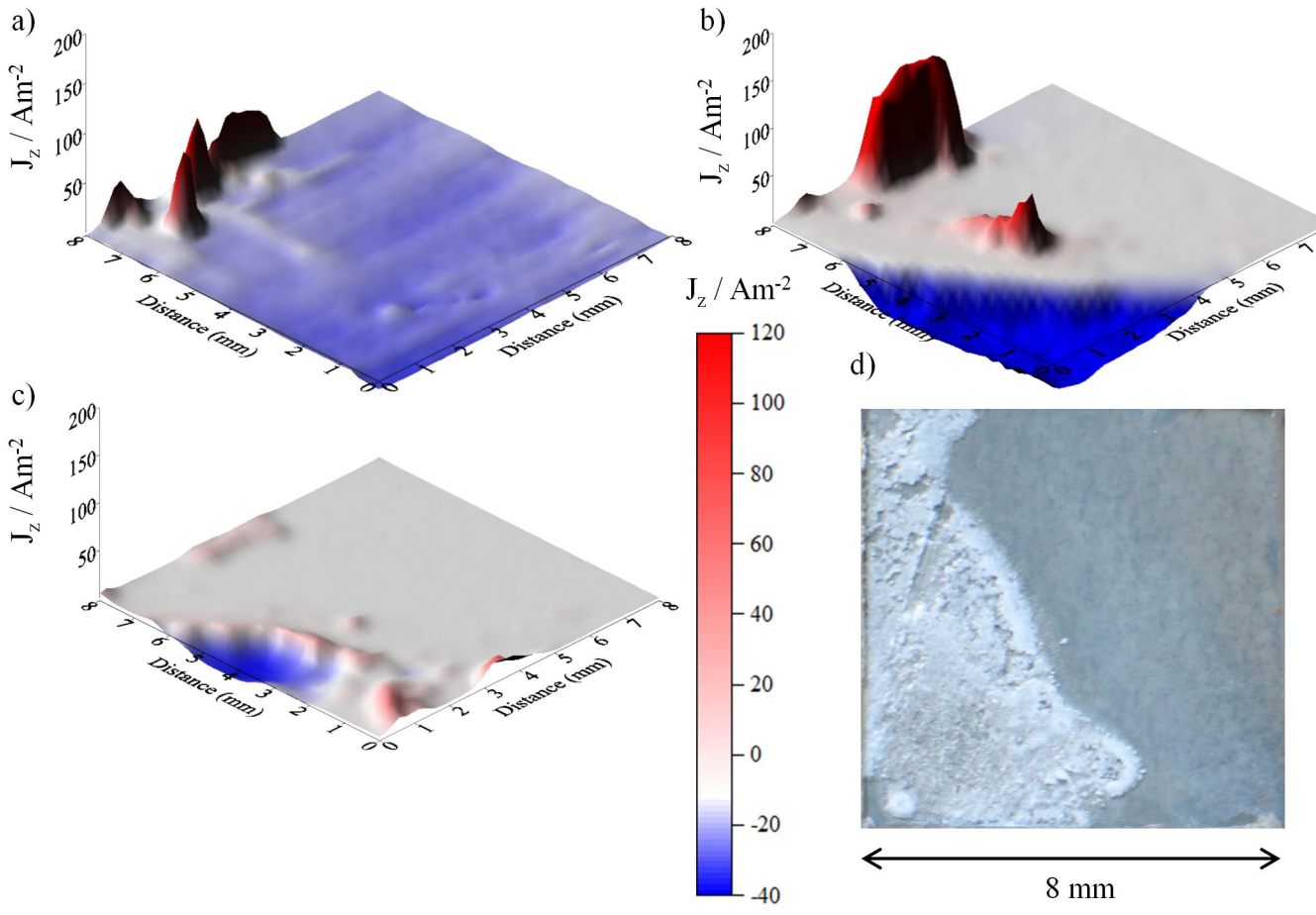
a)
b)
c)
d)
J_z / Am^{-2}
200
150
100
50
Distance (mm)
0
1
2
3
4
5
6
7
8
J_z / Am^{-2}
120
100
80
60
40
20
0
-20
-40
8 mm

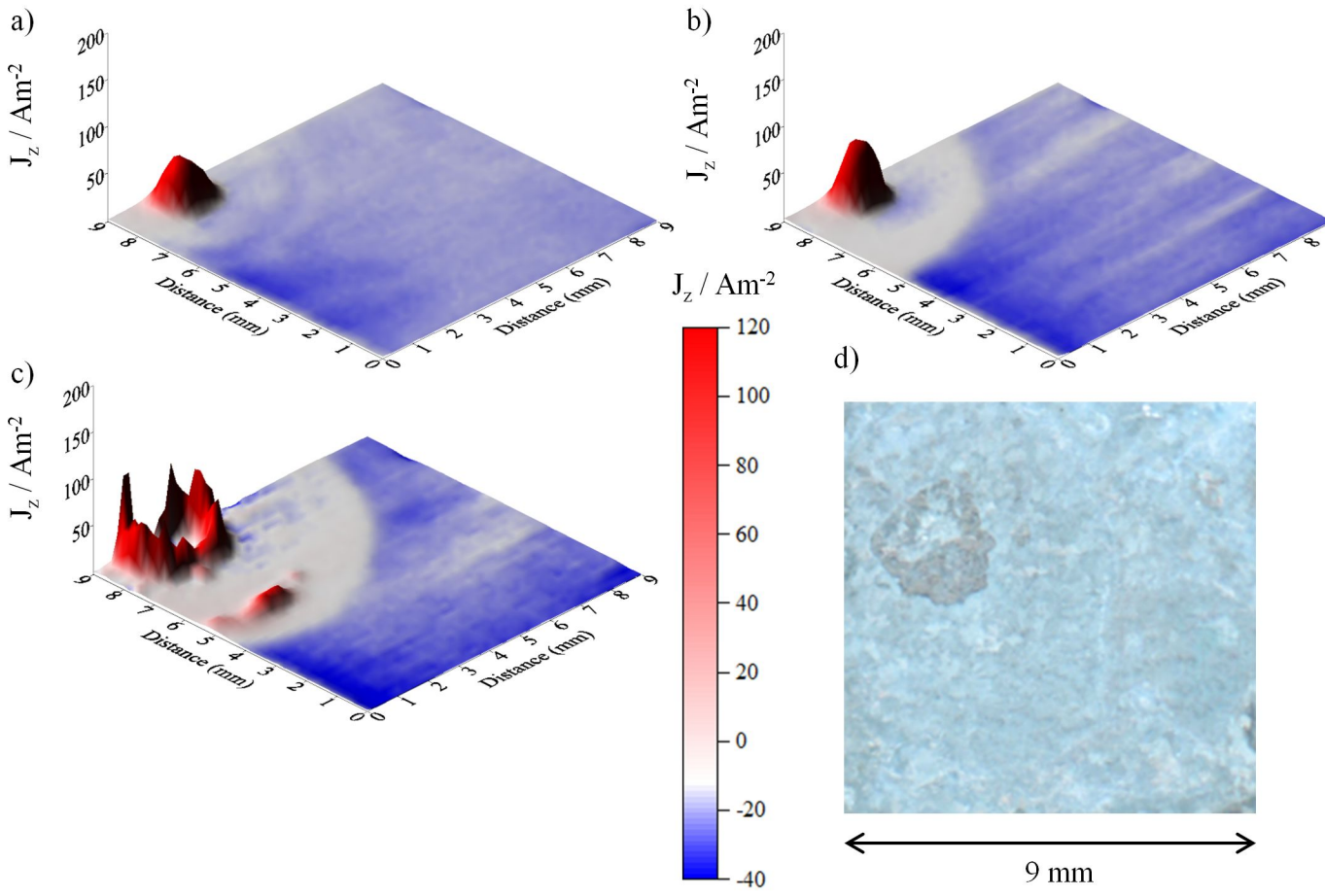
a)
b)
c)
d)
J_z / Am^{-2}
200
150
100
50
Distance (mm)
0 1 2 3 4 5 6 7 8 9
J_z / Am^{-2}
120
100
80
60
40
20
0
-20
-40
9 mm

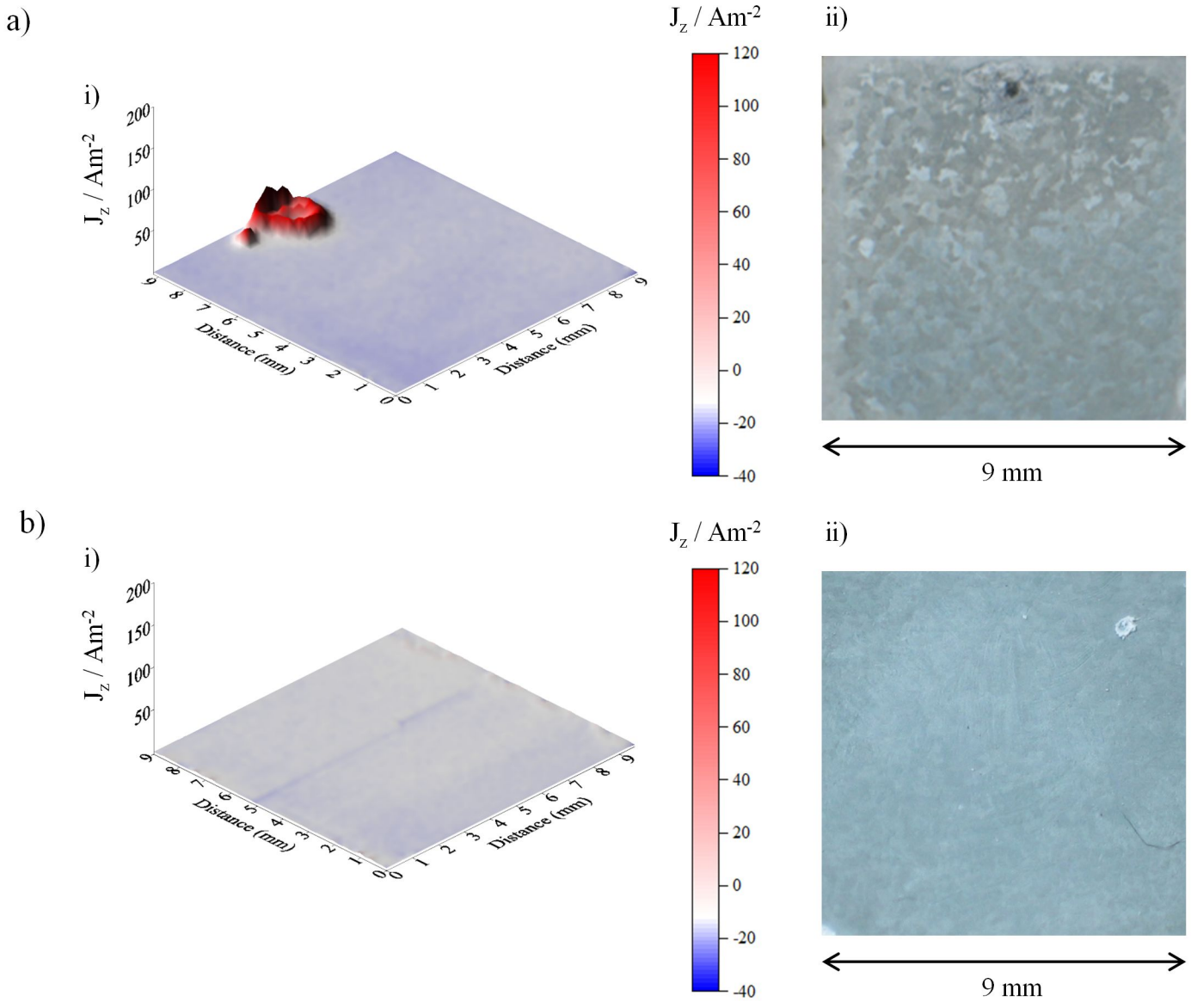
a)
i)
J_z / Am^{-2}
200
150
100
50
Distance (mm)
Distance (mm)
J_z / Am^{-2}
120
100
80
60
40
20
0
-20
-40
ii)
9 mm
b)
i)
J_z / Am^{-2}
200
150
100
50
Distance (mm)
Distance (mm)
J_z / Am^{-2}
120
100
80
60
40
20
0
-20
-40
ii)
9 mm

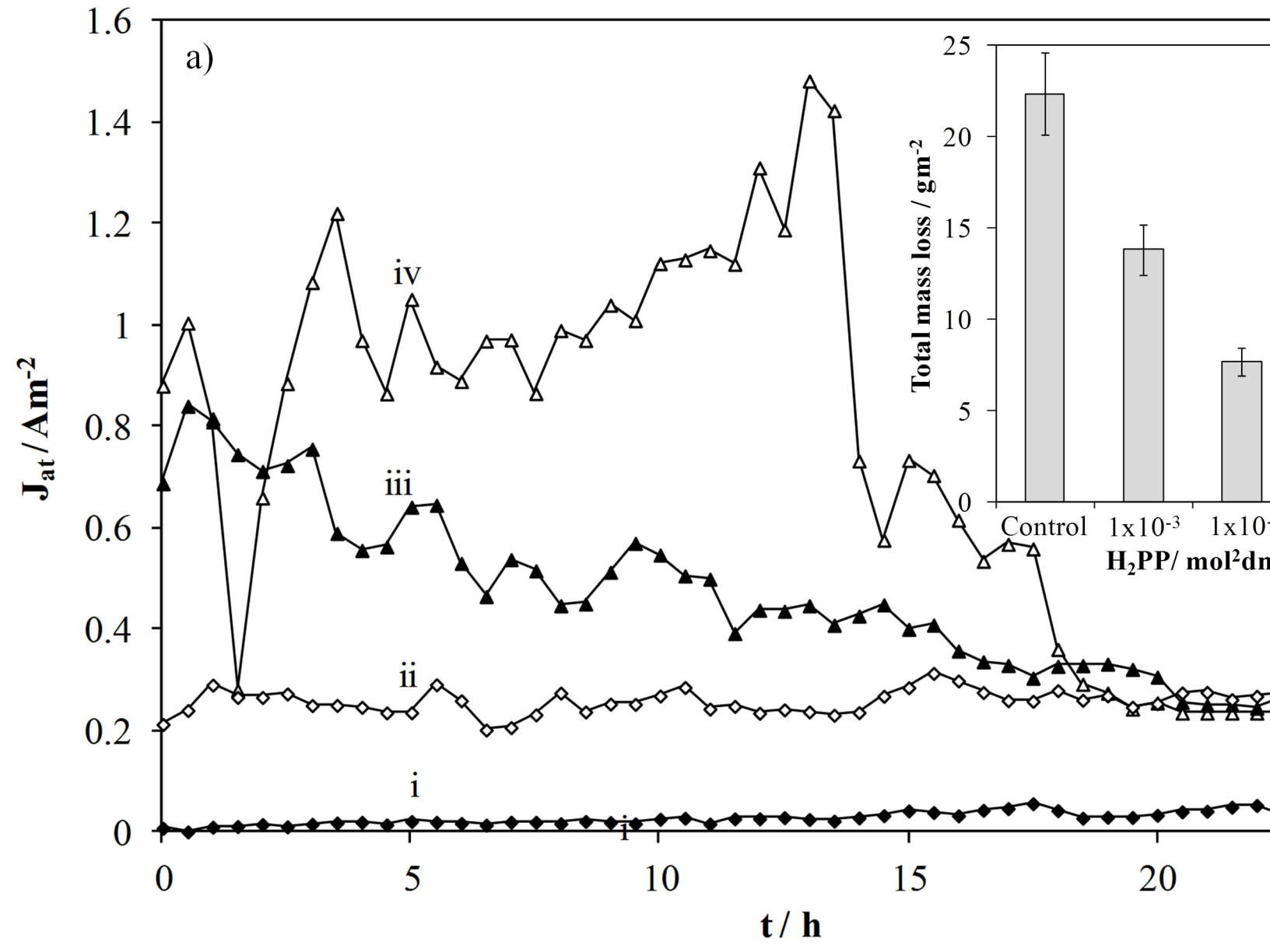
a)
1.6
1.4
1.2
1
0.8
0.6
0.4
0.2
0
J_{at} / Am^{-2}
iv
iii
ii
i
0
5
10
15
20
t / h
25
20
15
10
5
0
Total mass loss / gm^{-2}
Control
1x10^{-3}
H_2PP/ mol^{2}dm

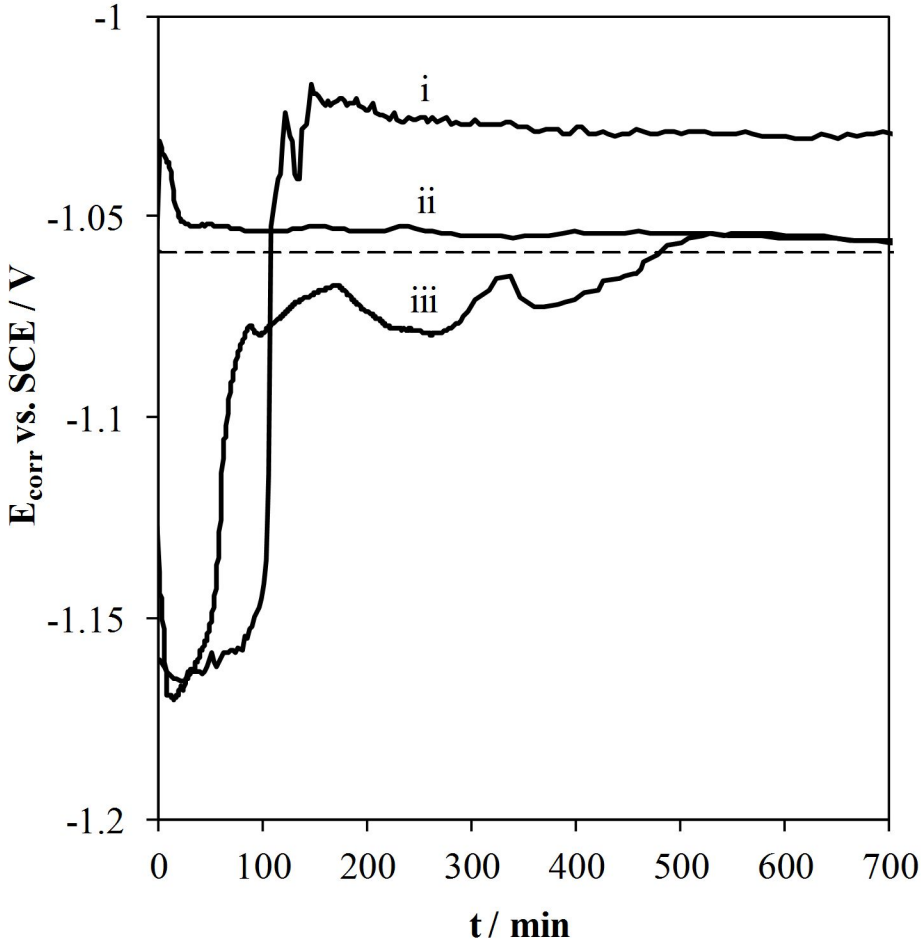
-1
-1.05
-1.1
-1.15
-1.2
0
100
200
300
400
500
600
700
i
ii
iii
E_corr vs. SCE / V
t / min

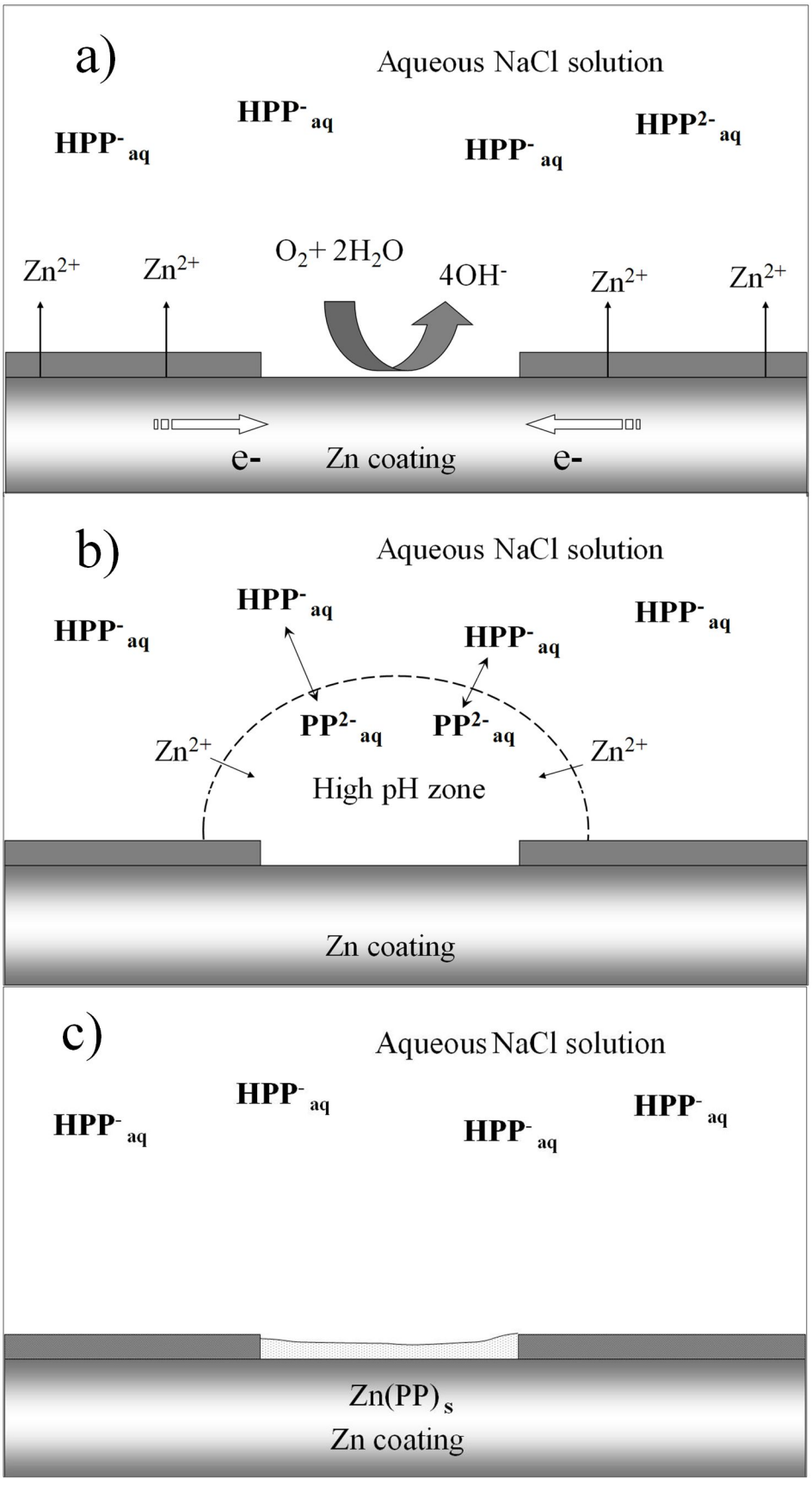
a)
Aqueous NaCl solution
HPP- aq
HPP- aq
HPP- aq
HPP2- aq
Zn2+
Zn2+
O2+ 2H2O
4OH-
Zn2+
Zn2+
e-
Zn coating
e-
b)
Aqueous NaCl solution
HPP- aq
HPP- aq
HPP- aq
HPP- aq
PP2- aq
PP2- aq
Zn2+
Zn2+
High pH zone
Zn coating
c)
Aqueous NaCl solution
HPP- aq
HPP- aq
HPP- aq
Zn(PP) s
Zn coating

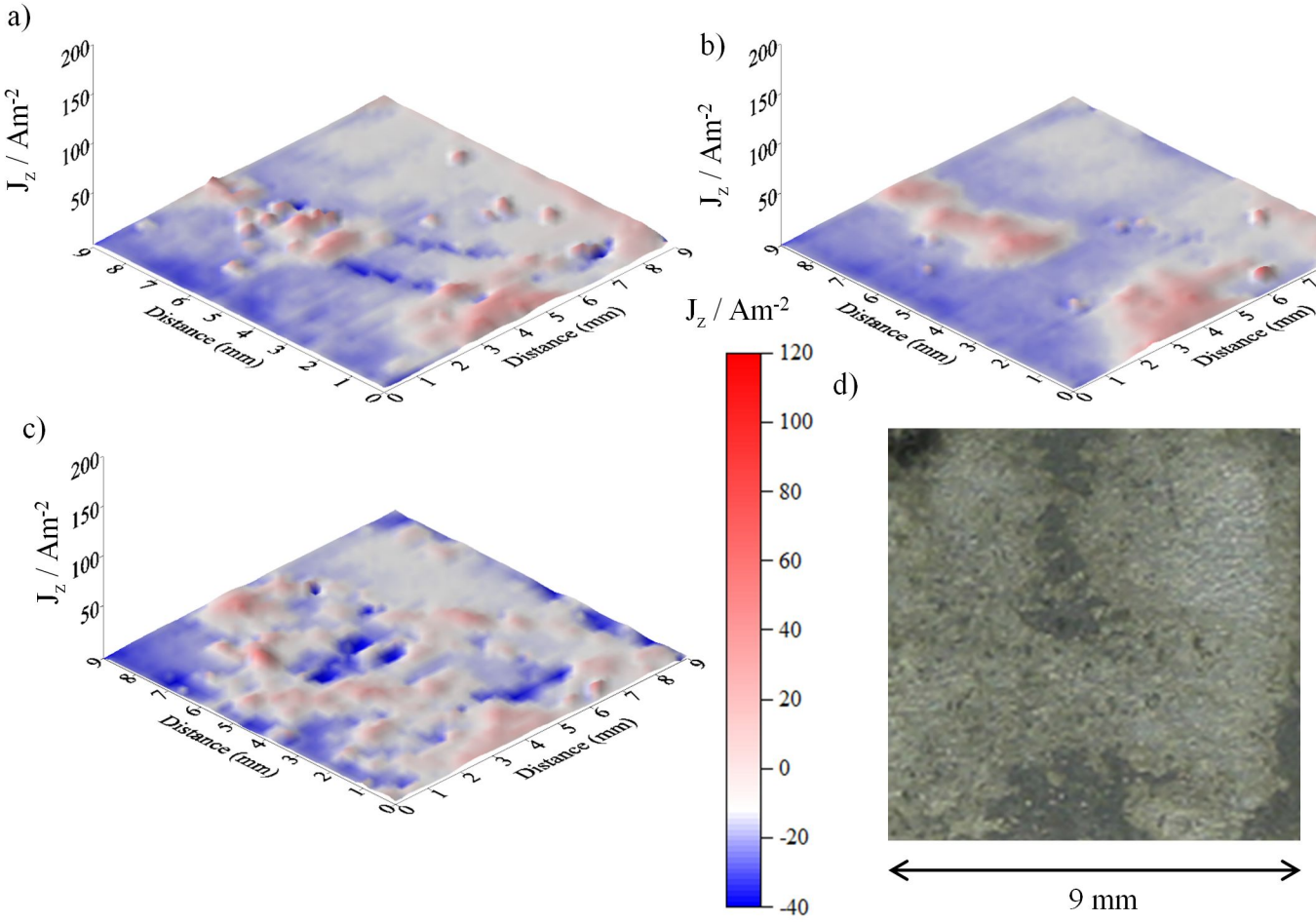
a)
b)
c)
d)
J_z / Am^{-2}
200
150
100
50
0
Distance (mm)
0 1 2 3 4 5 6 7 8 9
J_z / Am^{-2}
120
100
80
60
40
20
0
-20
-40
9 mm

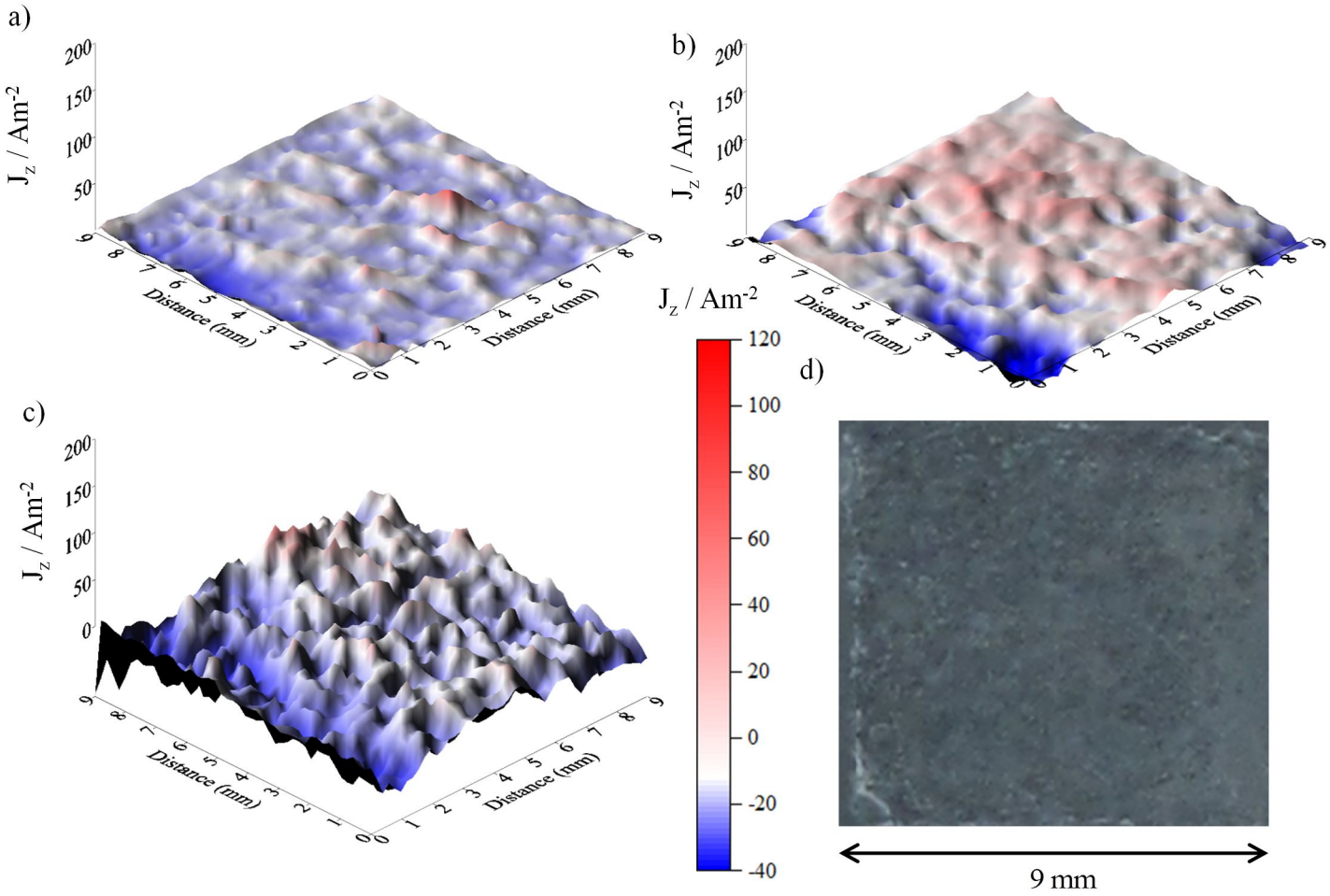
a)
b)
c)
d)
J_z / Am^{-2}
200
150
100
50
0
-9
-8
-7
-6
-5
-4
-3
-2
-1
0
1
2
3
4
5
6
7
8
9
Distance (mm)
120
100
80
60
40
20
0
-20
-40
9 mm

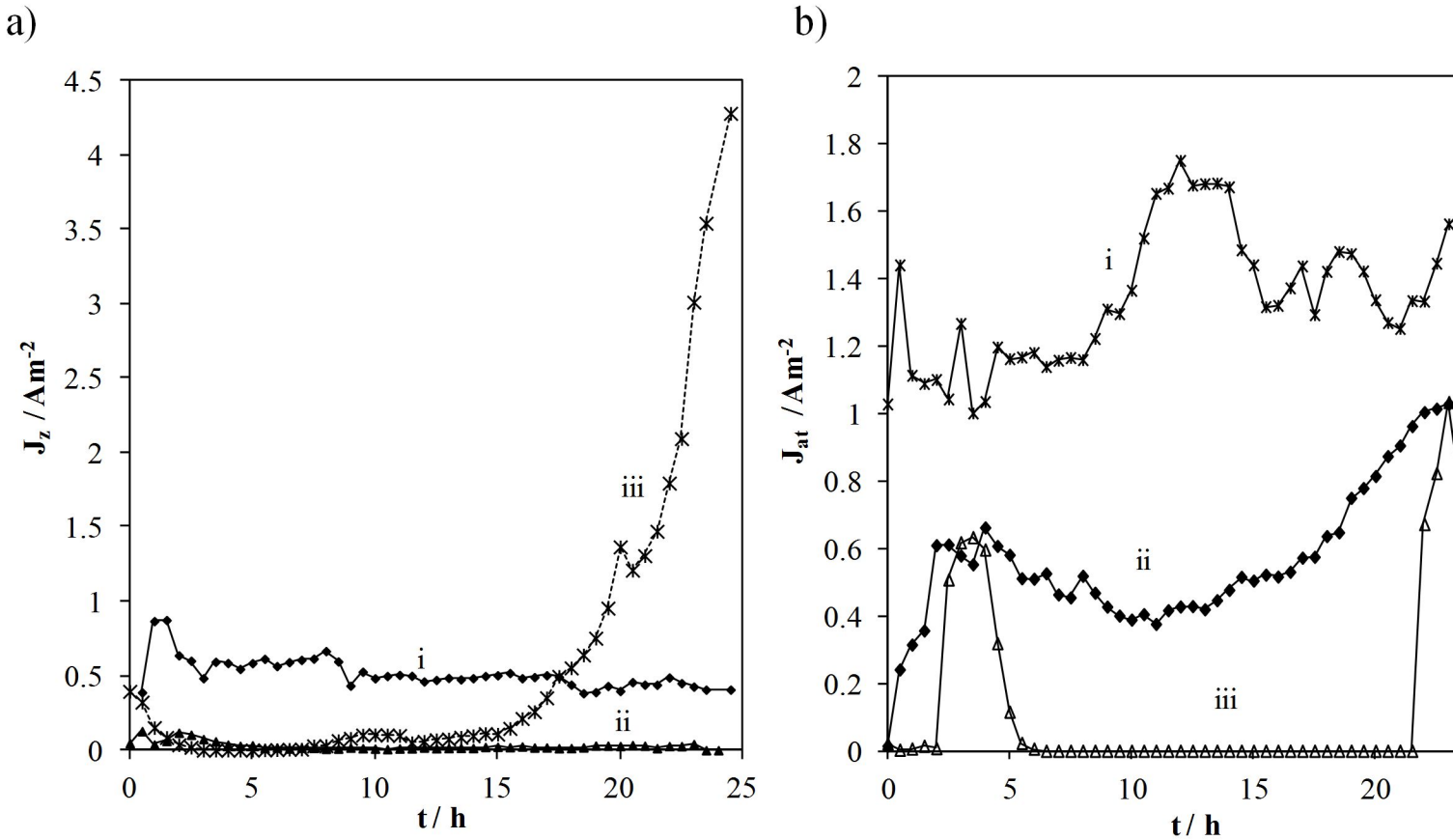
a)
b)
J_z /Am^{-2}
J_{at} /Am^{-2}
t / h
t / h
i
ii
iii
i
ii
iii

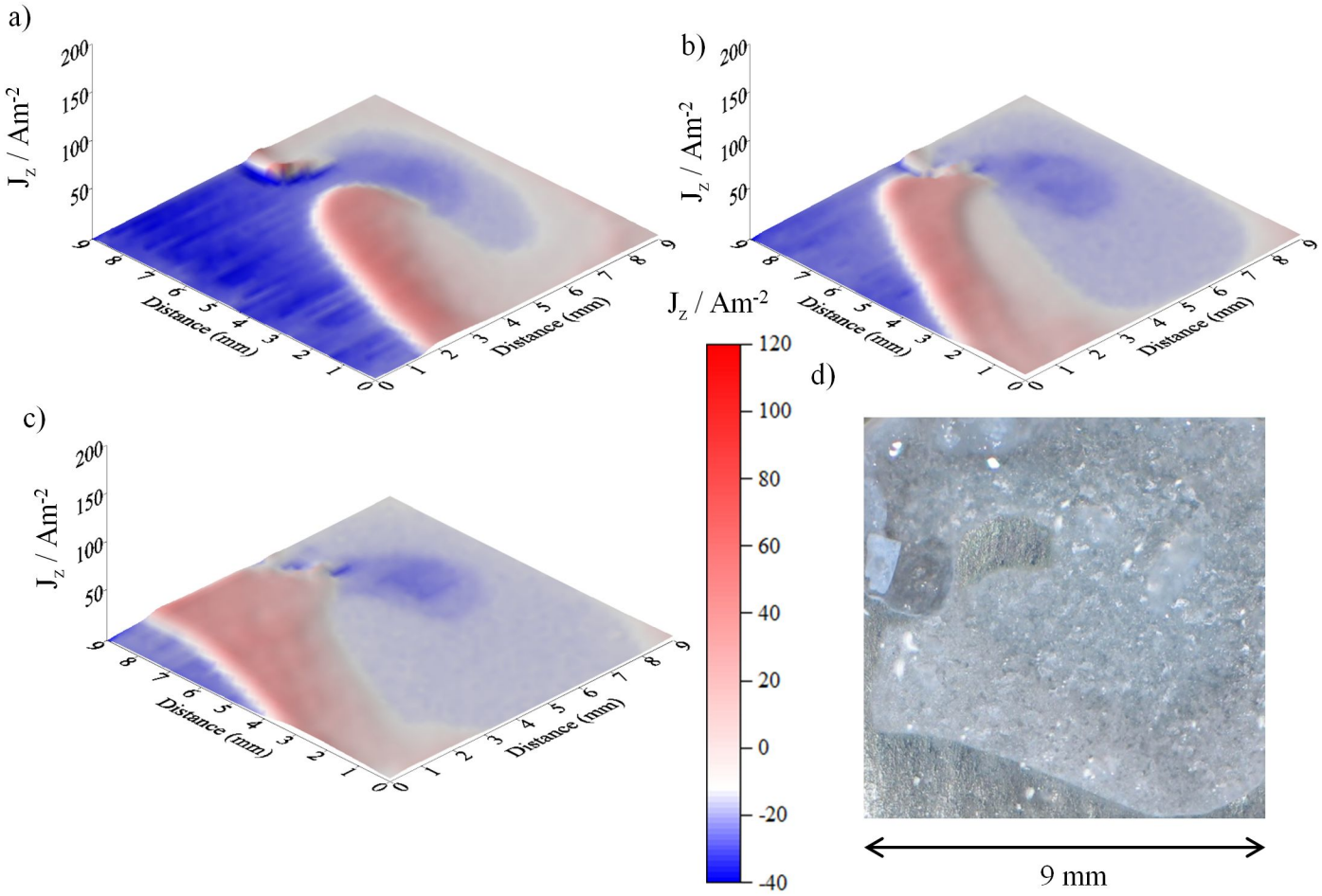
a)
b)
c)
d)
J_z / Am^{-2}
200
150
100
50
Distance (mm)
0 1 2 3 4 5 6 7 8 9
120
100
80
60
40
20
0
-20
-40
9 mm

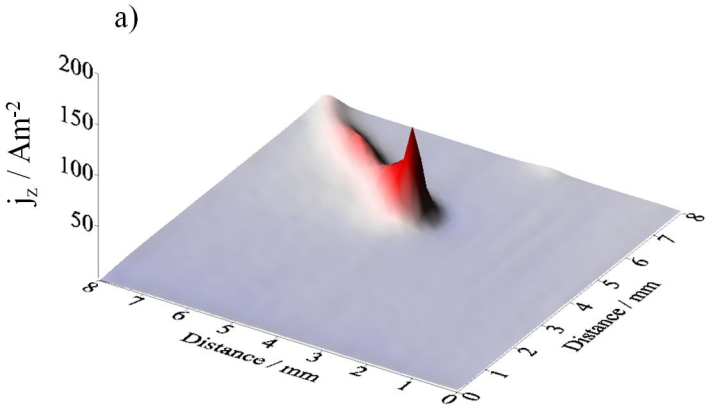
a)
j_z / Am^{-2}
200
150
100
50
Distance / mm
Distance / mm

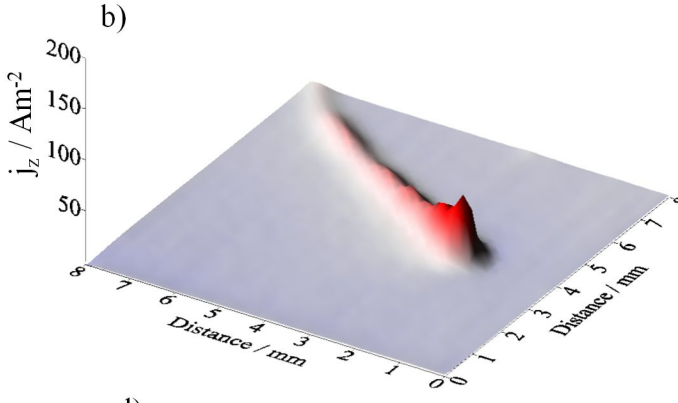
b)
j_z / Am^{-2}
200
150
100
50
Distance / mm
Distance / mm

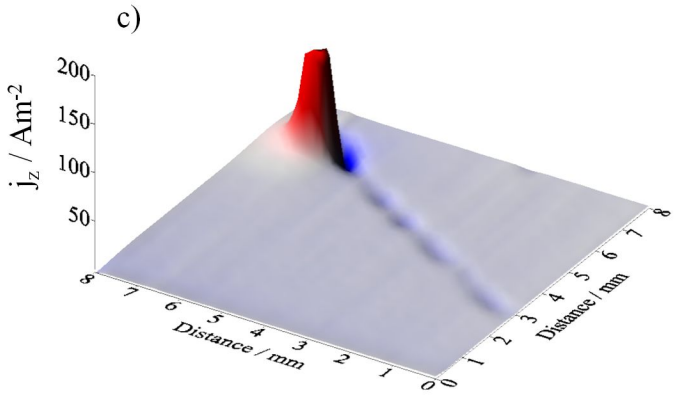
c)
j_z / Am^{-2}
200
150
100
50
Distance / mm
Distance / mm

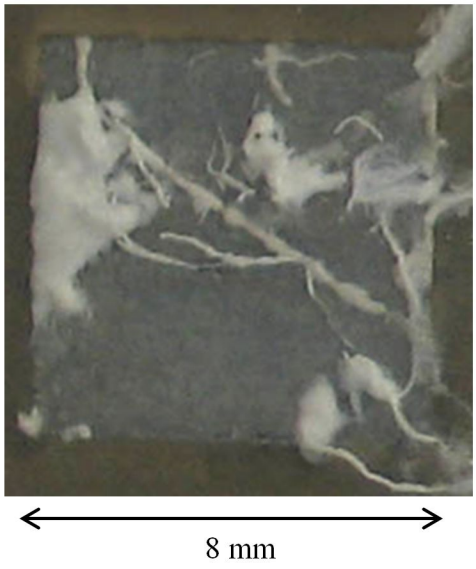
d)
8 mm

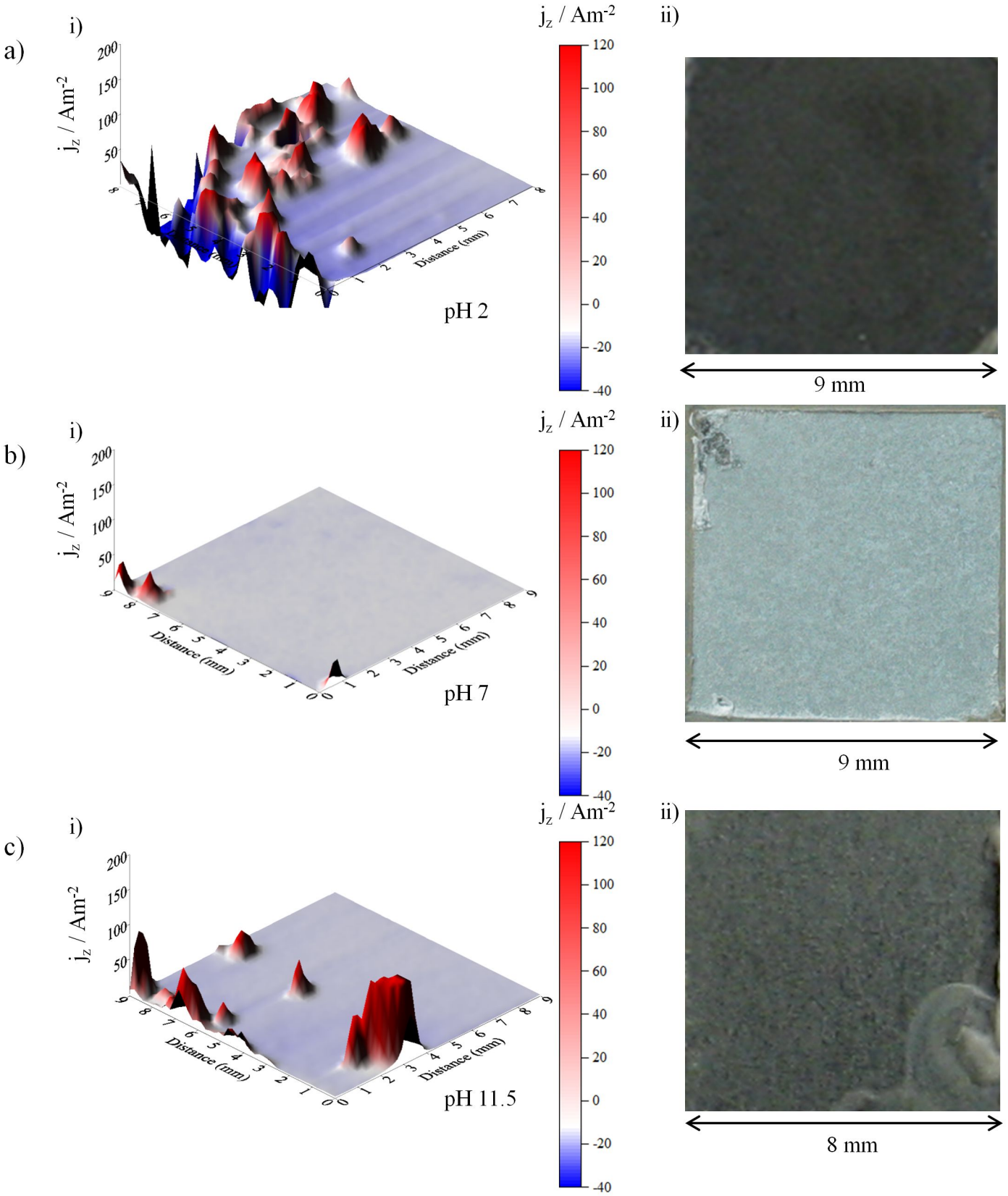
a)
i)
j_z / Am^{-2}
200
150
100
50
Distance (mm)
pH 2
j_z / Am^{-2}
120
100
80
60
40
20
0
-20
-40
ii)
9 mm
b)
i)
j_z / Am^{-2}
200
150
100
50
Distance (mm)
Distance (mm)
pH 7
j_z / Am^{-2}
120
100
80
60
40
20
0
-20
-40
ii)
9 mm
c)
i)
j_z / Am^{-2}
200
150
100
50
Distance (mm)
Distance (mm)
pH 11.5
j_z / Am^{-2}
120
100
80
60
40
20
0
-20
-40
ii)
8 mm

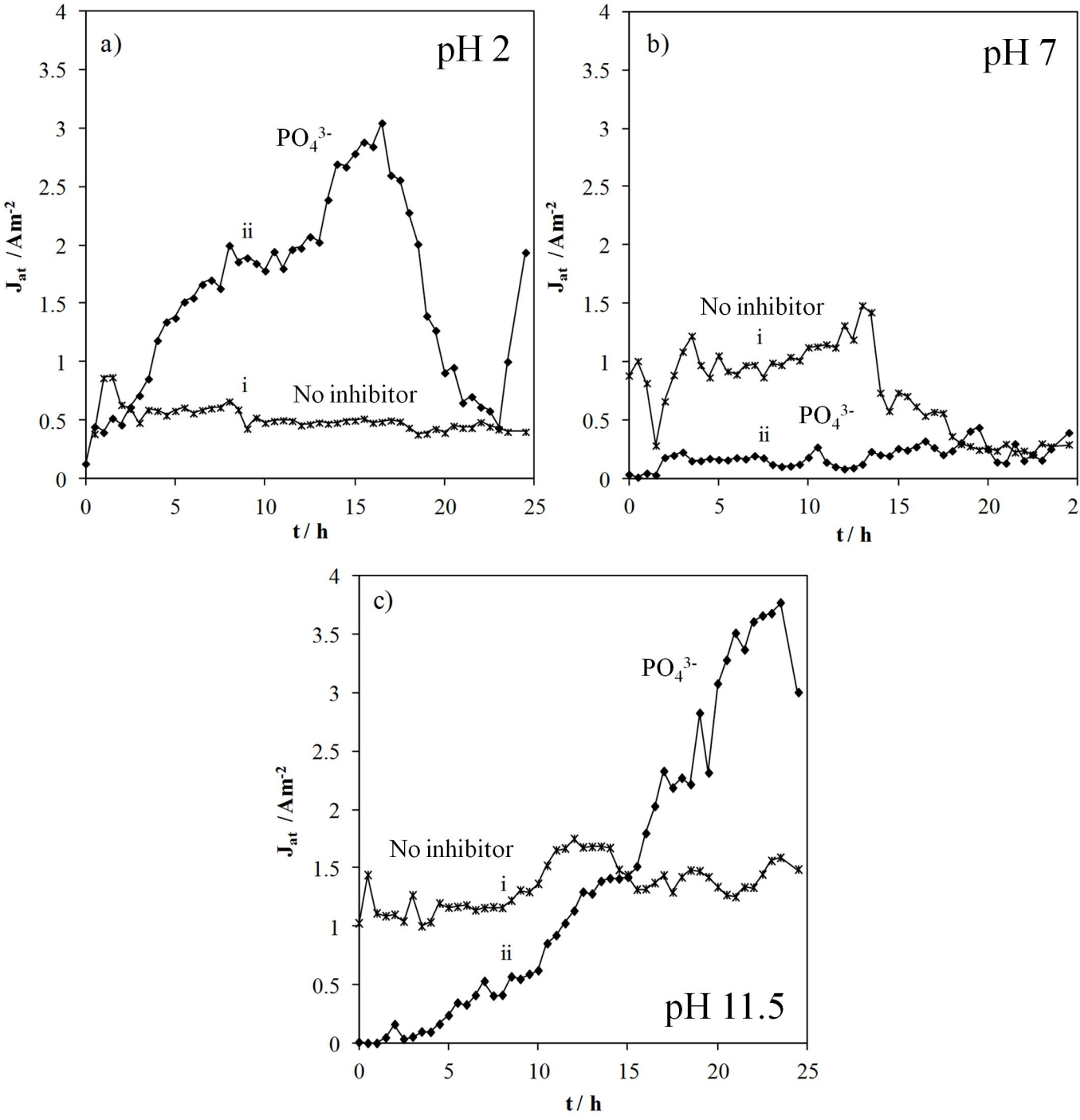
a)
pH 2
PO_4^{3-}
ii
i
No inhibitor
J_{at} /Am^{-2}
t / h
b)
pH 7
No inhibitor
i
PO_4^{3-}
ii
J_{at} /Am^{-2}
t / h
c)
PO_4^{3-}
No inhibitor
i
ii
pH 11.5
J_{at} /Am^{-2}
t / h

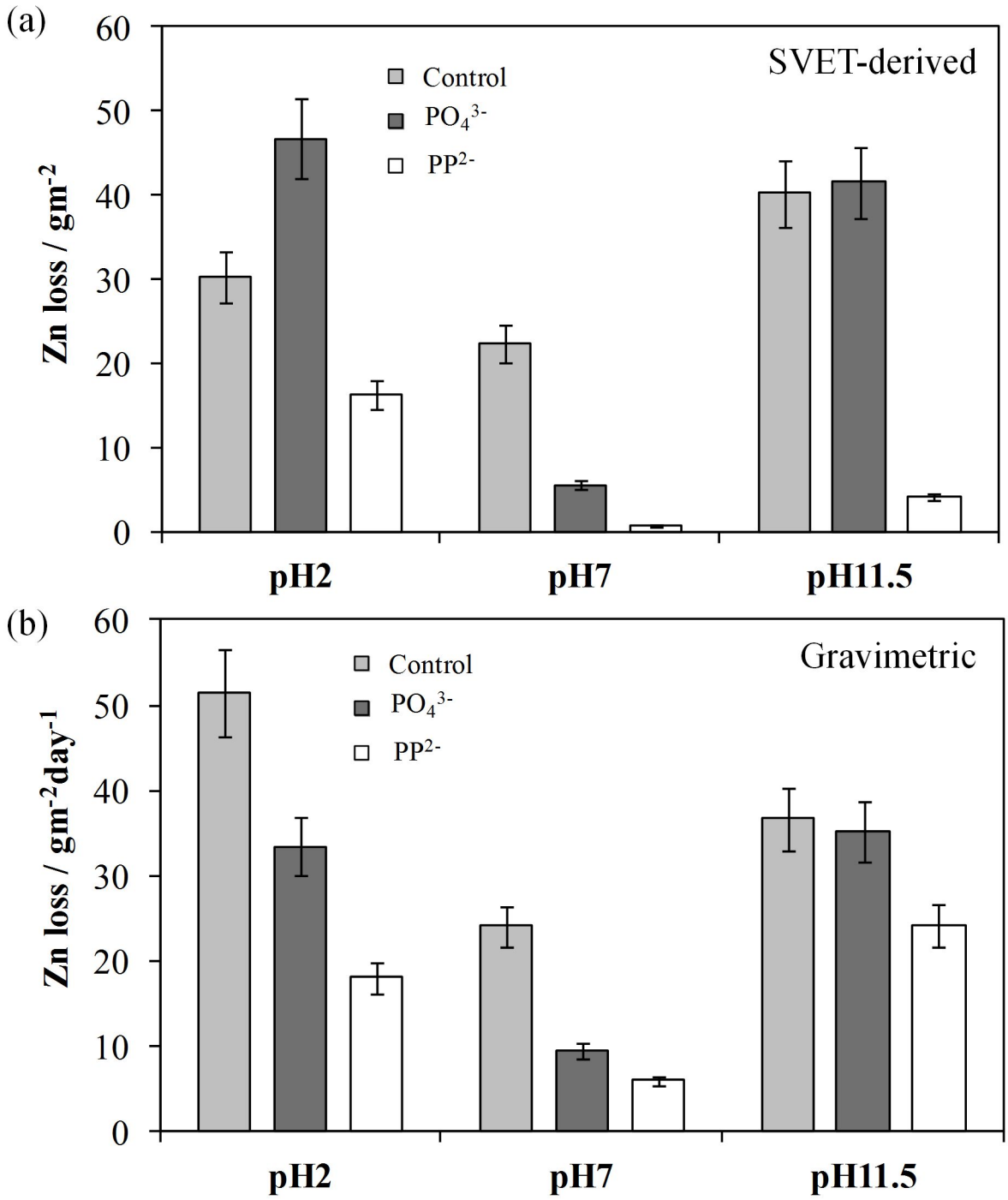
(a)
SVET-derived
Control
PO_4^{3-}
PP^{2-}
Zn loss / gm^{-2}
0
10
20
30
40
50
60
pH2
pH7
pH11.5
(b)
Gravimetric
Control
PO_4^{3-}
PP^{2-}
Zn loss / $gm^{-2}day^{-1}$
0
10
20
30
40
50
60
pH2
pH7
pH11.5

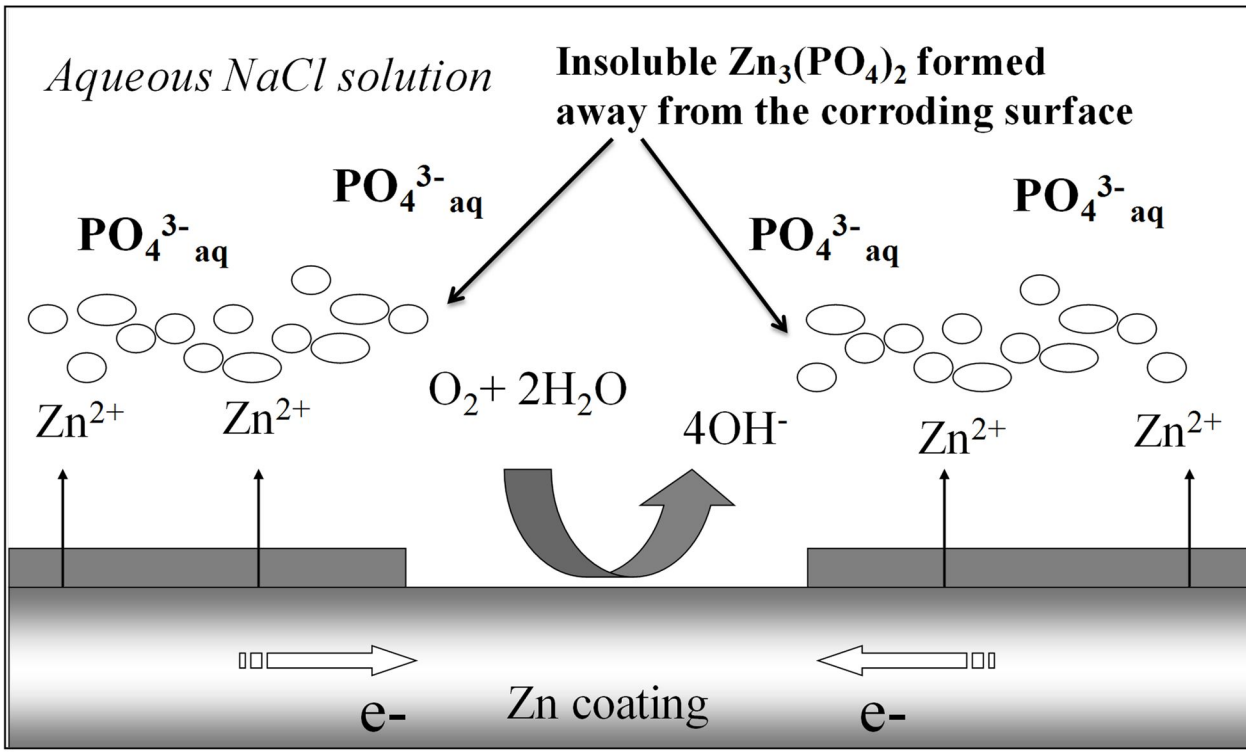
Aqueous NaCl solution
Insoluble $Zn_3(PO_4)_2$ formed away from the corroding surface
$PO_4^{3-}{}_{aq}$
$PO_4^{3-}{}_{aq}$
$PO_4^{3-}{}_{aq}$
$PO_4^{3-}{}_{aq}$
Zn^{2+}
Zn^{2+}
$O_2 + 2H_2O$
$4OH^-$
Zn^{2+}
Zn^{2+}
e-
Zn coating
e-